BeBeC-2026-S01

ACTIVE FUNCTIONAL BEAMFORMING

Robert P. Dougherty[1]
[1]OptiNav, Inc.
1414 127th PL NE #106, 98005, Bellevue, WA, USA

ABSTRACT

Functional Beamforming is adapted to the case of active medical ultrasound data. The new method appears formally similar to FB for the passive case, but is different in important ways because of the active, pulsed, nature of the data. For each grid point, the vector for the beamforming is created by sampling each channel at only the time corresponding to an echo from that grid point. This leads to very high resolution, including in depth, but does not produce a full Cross Spectral Matrix for methods such as FB to take advantage of. There have been academic efforts to create a full CSM for adaptive beamforming, actually one for each grid point, but the approach here is to work with the rank-1 CSM that is available and limit ν to avoid loss of signal. The method was tested on a set of publicly available ultrasound data and shows a big improvement in contrast using $\nu = 1.2 - 1.5$. The method improves medical ultrasound results by reducing speckle with no added computational effort. The dataset used is a case of multiple plane waves, and each combination of plane wave and transducer is treated as a separate channel. For completeness, equations for a corresponding version of Robust Adaptive Beamforming are also given. It is likely that FB method described here will also lower the sidelobes for sparse 2D ultrasound arrays, leading to another big improvement in the technology.

1 INTRODUCTION

In medical ultrasound, an array of transducers is fired to create a pulse of sound. Some of the sound reflects from inhomogeneities in the body of the patient called echo generators. The reflected sound is received by the transducers and used in a beamforming process to form a spatial map of echogenicity which has medical diagnostic value. The usefulness of the map depends on the resolution and the dynamic range, or contrast, as well as the frame rate. In simplistic beamforming, the resolution is limited by the size of the array relative to the acoustic wavelength. The contrast is limited by speckle which is caused by diffuse reflection by the microscopic structure of cells. One approach to the beamforming is to use analog beamforming for both the transmit and receive phases of the process. This gives relatively high dynamic range because the beamforming spatial filtering is applied twice, first on transmit and then on receive. The major disadvantage of this approach is that it is necessary to scan the transmit beam and

wait for the round-trip sound propagation before moving to the next grid point in the image. The frame rate is therefore limited, interfering with the ability to image dynamic processes such as movement of blood vessel walls. In the newer scenario, an unfocused wave, such as plane wave, is created and the image formation is done using digital beamforming of the received data. Assuming the digital beamforming can keep up, this increases the potential frame rate to the reciprocal of one round-trip travel time. In this method, the dynamic range of the beamforming becomes more critical because the redundancy of using two beamforming steps has been removed. More recently, a compromise method called plane wave compounding [1] has been developed in which a frame uses dozens of plane waves delivered at different angles (Fig. 1). The receive beamforming then has a larger effective number of channels to work with: NL, where N is the number of receive transducers and L is the number of plane waves. In applications of passive beamforming in other fields such as radio astronomy and aeroacoustics, several advanced methods have been developed to increase the resolution and dynamic range relative to simplistic beamforming. These include Robust Adaptive Beamforming (RAB) [2], deconvolution methods such as CLEAN and DAMAS, and Functional Beamforming (FB) [3,4] Deconvolution may not be well-suited to clinical ultrasound due to its slow speed. Academic papers about applying RAB describe methods that require constructing and inverting a different covariance matrix for each point in the beamforming grid [5-6]. Deep learning has been applied [7].

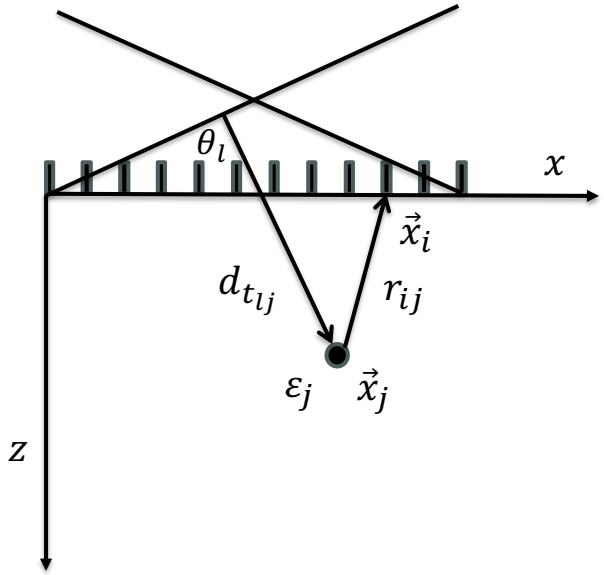

Fig. 1. The setup for multiple plane wave ultrasound. The transmit and receive delays for grid point j and transducer i with plane wave l are shown.

2 PICMUS

The Plane-Wave Imaging Challenge in Medical Ultrasound, PICMUS [8], was a contest to apply advanced beamforming methods to several datasets to improve the results compared with DAS and the other contestants. CPU time was not part of the metric. The datasets include synthetic and measured data for two parts of a phantom as well as two sets of in-vivo data for a carotid artery of a health volunteer. The data remain publicly available and were used for the results here. Sample RF and IQ beamforming MATLAB scripts are also given, and these were a big help in understanding how ultrasound beamforming works, although the work here was

done in Java, not MATLAB. PICMUS uses the same setup for all of the datasets. The experimental data was taken with a linear array transducer from Verasonics (Fig. 2). The center wavelength is 0.30 mm, as is the spacing between the 128 transducers. The beamforming grid was specified to match the width of the array, 38.4 mm, in the x direction and to extend from 5 to 50 mm in z. The resolution in the beamforming maps is about 0.4 mm in both directions across the entire grid, which never could have happened in passive beamforming.

Fig. 2. Verasonics L11-4v linear array transducer.
https://normit.no/normit/display_resource.php?resource_id=32

The PICMUS data specifications are:

Verasonics Vantage 256 platform and the linear L11-4v probe
75 steered Plane-Waves covering the angle span from -16° to 16°
Pitch 0.30 mm
Element width 0.27 mm
Element height 5 mm
Elevation focus 20 mm
Number of elements 128
Aperture width 38.4 mm
Transmit frequency 5.208 MHz
Sampling frequency 20.832 MHz
Pulse bandwidth 67%
Excitation 2.5 cycles

3 ULTRASOUND BEAMFORMING

The speed of sound of longitudinal waves in the body, c, is about 1540 m/s. An excitation of the transducer array creates a disturbance with a waveform $f(t) = e^{-\left(\frac{t}{b}\right)^2} cos(\omega_0 t)$, where $\omega_0 = 2\pi f_0$ and the modulation frequency is f_0. The pulse length, b, is a small number of periods of the modulation frequency. For the PICMUS data, f_0 = 5.208 MHz and b = 2.5 samples. (For the synthetic resolution data, b appears to be 1.5 samples.) Suppose there are Mgrid points, $\vec{x}_j, j = 1, \dots, M$. Each grid point is characterized by echogenicity ε_j. The echos

are typically caused by nonuniformities in density or compressibility at $\vec{x}_j$. The goal is to make a beamform image (called a B-mode image) that shows the echogenicity in dB, $20log_{10}|\varepsilon_j|$, over the grid. There are L plane waves transmitted into the medium at different angles. Excitation l reaches $\vec{x}_j$ after a transmission delay $d_{t_{lj}}$. Plane wave l has $d_{t_{lj}} = \frac{(z_j \cos\theta_l + x_j \sin\theta_l)}{c}$, where θ_l is the angle between the transducer array and the wave and x_j and z_j are components of $\vec{x}_j$. Upon reaching the echogenerator at $\vec{x}_j$, the excitation gives rise to a reflected wave that propagates back to the transducer array. Suppose there are N transducers, now considered as microphones, located at $\vec{x}_i, i = 1, \dots, N$. Notationally, the location subscript index i or j differentiates a transducer position, $\vec{x}_i$, from a beamforming grid point, $\vec{x}_j$. The symbol i is also used for $\sqrt{-1}$ with the physics-affiliated sign convention in which a plane wave would be $e^{i(\vec{k}\cdot\vec{x}-\omega t)}$. The reception delay between the echo source at $\vec{x}_j$ and the microphone at $\vec{x}_i$ is $\frac{r_{ij}}{c}$, were $r_{ij} = \|\vec{x}_j - \vec{x}_i\|$. The Radio Frequency (RF) signal received at microphone i by scattering of excitation l by echogenerator j is modeled as $\varepsilon_j f(t - d_{ilj})$, where the total delay is $d_{ilj} = d_{t_{lj}} + \frac{r_{ij}}{c}$. The amplitude factors for the outward and return propagation are omitted for simplicity. In a linear 1D ultrasound probe, the transducer crystals are in the plane $z = 0$, are spaced in the x-direction, and are tall in the y-direction and focused in y with the intention that the image represents a single y plane. The height of the transducers in the L11-4v probe is 5 mm and they have an optimum focus at 20 mm near the center of the z range of the images, 5-50 mm.

Assuming weak scattering and the simplified geometry, the model for the RF signal (Fig. 1) received at microphone i from shot l is

$$r_{il}(t) = \sum_{j=1}^{M} \varepsilon_j f(t - d_{ilj}) = \sum_{j=1}^{M} \varepsilon_j e^{-\left(\frac{t-d_{ilj}}{b}\right)^2} cos\left(\omega_0(t - d_{ilj})\right)$$
$$i = 1, \dots, N; l = 1, \dots, L. \qquad (1)$$

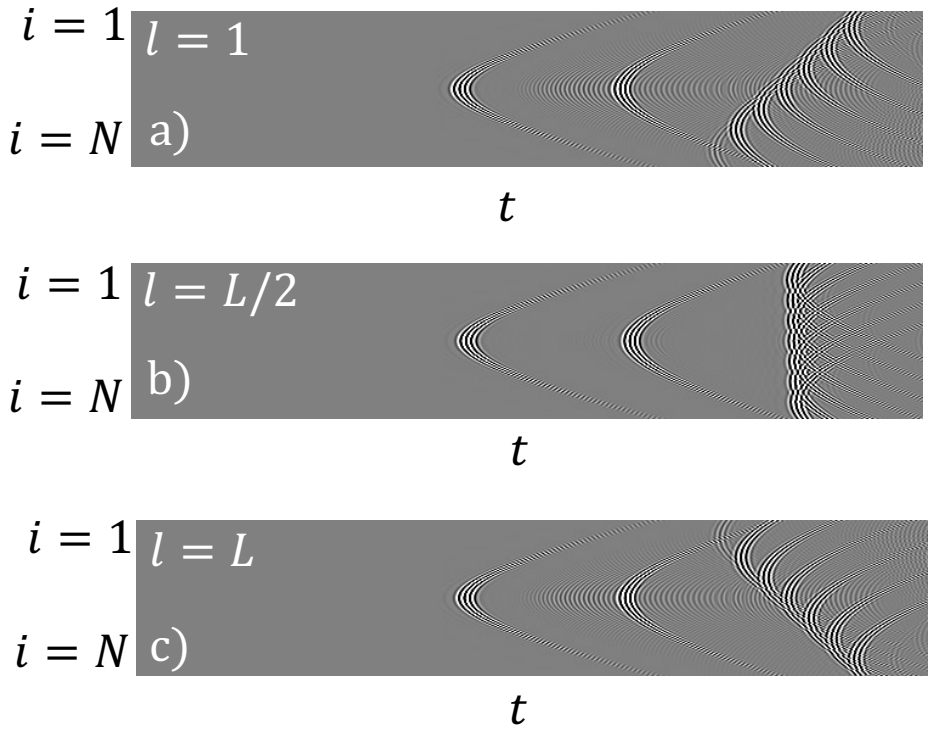

Fig. 3. Radio Frequency (RF) ultrasound data from the synthetic resolution case in the PICMUS challenge.

The goal is to invert this model to determine the ε_j. Consider a grid point j and estimate ε_j by a beamforming procedure. The simplest beamforming method, Delay And Sum beamforming using RF data (RFDAS) is obtained by evaluating $p_{il}(t)$ at d_{ilj} (often using cubic spline interpolation), summing over i and l, and taking the magnitude-squared as indicated in Eq. (2):

$$RFDAS_j = \left| \sum_{l=1}^{L} \sum_{i=1}^{N} w_{ij} r_{il}\left(d_{ilj}\right) \right|^2 \tag{2}$$

Here a normalized weight factor, or apodization w_{ij} is introduced to define a fixed f-number, depth to aperture size ratio, or otherwise tune the beamforming. Processing at f/1.75 was performed in this work. An example formula for w_{ij} is

$$w_{ij} = \frac{1}{W_j} e^{-\left(\frac{x_{j'} - x_i}{\sqrt{2}\frac{z_j}{f\#}}\right)^2} \tag{3}$$

The normalization W_j is chosen so that $\sum_{il=1}^{NL} w_{ij} = NL$.

Substituting Eq. (1) into Eq. (2) gives

$$RFDAS_j = \left| \sum_{j'=1}^{M} \varepsilon_{j'} \sum_{i=1}^{N} \sum_{l=1}^{L} w_{ij} e^{-\left(\frac{d_{ilj'} - d_{ilj}}{b}\right)^2} cos\left(\omega_0\left(d_{ilj'} - d_{ilj}\right)\right) \right|^2 \tag{4}$$

In the usual philosophy of beamforming, it is assumed that the sum over i and l is approximately 0 if $j \neq j'$. Both the Gaussian and the cosinusoidal factors in the formula suggest this.

Therefore

$$RFDAS_j \approx (NL)^2 \left|\varepsilon_j\right|^2 \tag{5}$$

DAS beamforming can be improved by operating in the frequency domain. A tuning angular frequency $\omega = 2\pi f$, which may or may not equal the modulation angular frequency ω_0, is selected. Digital IQ demodulation is applied to compute the in-phase and quadrature, I and Q, components of $p_{il}(t)$:

$$I_{i,l}(t) = LP\left[p_{i,l}(t)\cos\omega t\right] = \frac{1}{2}\sum_{j=1}^{M} \varepsilon_j e^{-\left(\frac{t-d_{ilj}}{b}\right)^2} \cos\left[(\omega-\omega_0)t + \omega_0 d_{ilj}\right] \tag{6}$$

$$Q_{i,l}(t) = LP\left[p_{i,l}(t)\sin\omega t\right] = \frac{1}{2}\sum_{j=1}^{M} \varepsilon_j e^{-\left(\frac{t-d_{ilj}}{b}\right)^2} \sin\left[(\omega-\omega_0)t + \omega_0 d_{ilj}\right] \tag{7}$$

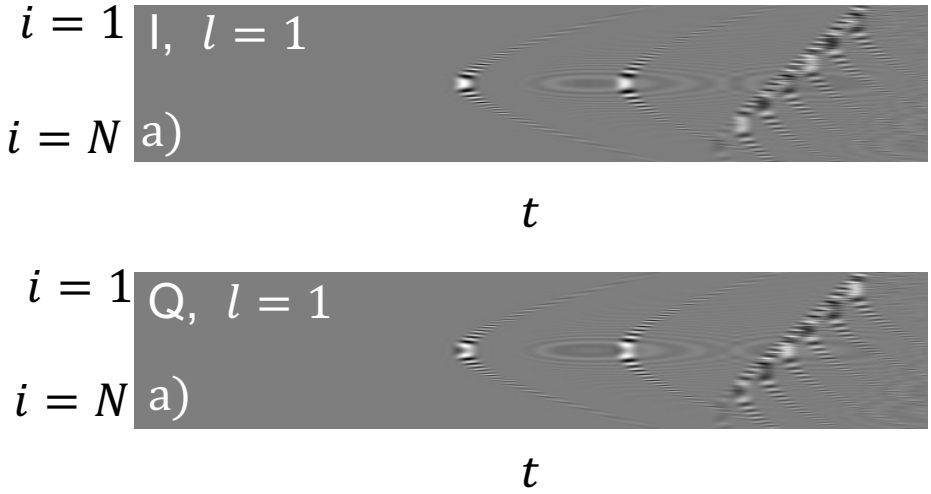

Fig. 4. In-phase and Quadrature, IQ, data corresponding to Fig. 3.

Here LP is a phaseless low-pass filter. It can be implemented, for example, by using a Butterworth filter twice, first in the forward direction and then in the reverse direction. The cutoff frequency of LP, $2\pi f_c$ is chosen to equal to or greater than or equal to f. The analysis bandwidth, $2(f_c - f)$, represents a frequency range centered on f over which ε is characterized.

Combining I and Q in complex notation gives a complex version of the data

$$P_{il}(t) \equiv I_{i,l}(t) + iQ_{i,l}(t) = \frac{1}{2}\sum_{j=1}^{M} \varepsilon_j e^{-\left(\frac{t-d_{ilj}}{b}\right)^2} e^{i\left[(\omega-\omega_0)t+\omega_0 d_{ilj}\right]} \tag{8}$$

Here $P_{il}(t)$ is a measured function of t for each microphone i and shot l. As before, the goal is to invert this model to determine the ε_j. The frequency-domain of the DAS beamforming beamforming expression for $\left|\varepsilon_j\right|^2$ is given in Eq. (9).

$$IQDAS_j = \left| \sum_{l=1}^{L} \sum_{i=1}^{N} w_{ij} e^{-i\omega d_{ilj}} P_{il}\left(d_{ilj}\right) \right|^2 \tag{9}$$

Equation (9) appears similar to the familiar formula for passive Frequency Domain Beamforming (FDBF) in that the pressure data for each sensor, i, is weighted by conjugate of a propagation phase factor, but is different in that the frequency-domain pressure at the sensor is also considered to be a function of absolute time and is evaluated at the delay time, like DAS. In passive FDBF, the pressure is considered random and statistically stationary. Time-averaging products of quantities considered to be samples of processes at different relative times, together with assumption that the process is ergodic are used to infer statistical properties of the sources in passive FDBF. The multiplicity of L shots in Eq. (5) is another difference from passive beamforming, and should not be confused with the independent averages in the passive case.

Substituting the model, Eq. (8), into the beamforming formula, Eq. (9) gives

$$IQDAS_{j'} = \left| \frac{1}{2} \sum_{j=1}^{M} \varepsilon_j \sum_{i=1}^{N} \sum_{l=1}^{L} w_{ij} e^{-\left(\frac{d_{ilj'} - d_{ilj}}{b}\right)^2} e^{i\omega_0\left(d_{ilj} - d_{ilj'}\right)} \right|^2 \tag{10}$$

Surprisingly, Eq. (10) does not explicitly depend on ω, the but the tuning frequency is still present behind the scenes because is controls the part of the spectrum of ε that is involved.

Again, it is assumed that the Gaussian terms are powerful enough that the sum over il can be taken to be zero if $j' \neq j$. This is special characteristic of active beamforming with the sharp pulse, and would not apply to passive beamforming. The assumption in passive beamforming that provides a similar separation of sources in the model is that assumption that sources at different grid points are mutually incoherent. Applying the assumption gives a result proportional to Eq. (5):

$$IQDAS_j \approx \frac{NL}{4} \left|\varepsilon_j\right|^2 \tag{11}$$

4 FORMULAS IN PASSIVE BEAMFORMING

In passive beamforming, a central element is the Cross Spectral Matrix (CSM), or covariance matrix. Let r be an n-vector of received sensor data. The CSM is $C = E[rr']$, which is usually estimated as a sample average

$$C = \frac{1}{N_b} \sum_{b=1}^{N_b} r_b r_b' \tag{12}$$

Here b refers to a snapshot or block of r, typically referring to Welch's method. The rank of C is at most N_b and it is reasonably important that the quantities averaged in Eq. (12) are in fact samples of rr'. Given a normalized steering vector, g, the conventional beamforming expression is

$$b = g'Cg \tag{13}$$

The Functional Beamforming (FB) expression is

$$b_\nu = \left[g' C^{\frac{1}{\nu}} g \right]^\nu \tag{14}$$

where $\nu \geq 1$. This matrix power $C^{\frac{1}{\nu}}$ is evaluated with the spectral mapping theorem by raising the (real, nonnegative) eigenvalues of C to the power $\frac{1}{\nu}$. The main benefit of BF is increasing

the dynamic range. Beamforming peaks are narrowed, but there is not an increase in resolution in the sense of separating nearby sources. As ν is increased, the output values of b_ν decrease monotonically. Assuming the steering vectors and the basic model are correct, Löwner-Heinz inequality can be used to show that the result will never go below the true source strength.

The Robust Adaptive Beamforming (RAB) formula traditionally begins with a regularized version of the weight vector from Minimum Variance Distortionless Response:

$$w = \frac{(C + \lambda I)^{-1} g}{g'(C + \lambda I)^{-1} g} \tag{15}$$

The addition of λI makes it possible to invert C when it is rank-deficient. Using this in place of the steering vector in Eq. (13) gives

$$b_{RAB} = \frac{1}{g'(C + \lambda I)^{-1} g} - \lambda \frac{g'(C + \lambda I)^{-2} g}{[g'(C + \lambda I)^{-1} g]^2} \tag{16}$$

The first term appears similar to FB with $\nu = -1$, although -1 is not a valid index for FB. A main benefit of RAB is increasing the resolution.

5 PROPOSED ADVANCED METHODS FOR ULTRASOUND

To try to improve the results in ultrasound beamforming, it is tempting to apply the the FB and RAB formulas to the active ultrasound data. First it is necessary to format the ultrasound data with its delay-based beamforming processing to expose a matrix that plays the role of C.

Starting with the IQ multiple plane wave data, define complex NL pressure and steering vectors according to

$$p[j] = \begin{bmatrix} P_1(d_{1j}) \\ \cdots \\ P_{NL}(d_{NLj}) \end{bmatrix} \tag{17}$$

$$g[j] = \frac{1}{\sqrt{NL}} \begin{bmatrix} w_{ij} e^{i\omega d_{1j}} \\ \cdots \\ w_{ij} e^{i\omega d_{NLj}} \end{bmatrix} \tag{18}$$

As in passive beamforming, g depends on the grid point, j. Unlike passive beamforming, p also depends on j and not on time, except in as much as the d_{ilj} are times. The interpretation of the dependence of $p[j]$ on j is that this is a complex pressure vector representing sound that comes "from" point j. The sharpness of the pulse and the sampling in Eq. (18) will have effectively eliminated sound from different points. It remains to be determined whether there is actually an echo source there. If there is, then the phases of the values in the different channels will beamform using the steering vector $g[j]$.

In addition to the proper echogenerator at $\vec{x}_j$, there is also the possibility of speckle source at $\vec{x}_j$. This is a group of microscopic structures (cells) in the area of $\vec{x}_j$ that combine to scatter waves in different directions with different phases, giving rise to a steering vector that is not parallel to $g[j]$ and consequently does not beamform as well as the echo source. This will be added to source model below. The delay sampling of the IQ data isolates the speckle source, as well as the echo source, to one grid point at a time in the beamforming.

The magnitude-squared beamforming expression becomes

$$IQDAS_j = (g'p)(g'p)^* = g'pp'g = g'C[j]g \tag{19}$$

where $C[j] = p[j]p'[j]$ is a rank-1 matrix.

Choosing $\omega = \omega_0$ from now on and combining Eqs. (8) and (17), the model for $p[j]$, before adding the speckle source, is

$$p[j] = \sum_{j'} \varepsilon_{j'}\, h_{j'} \tag{20}$$

where, $h_{j'}$ is the NL vector

$$h_{j'} = \frac{1}{2}\begin{bmatrix} \cdots \\ e^{-\left(\frac{d_{ilj}-d_{ilj'}}{b}\right)^2} e^{i\omega d_{ilj'}} \\ \cdots \end{bmatrix} \tag{21}$$

The assumption about the effect of the Gaussians is that, within a beamforming expression, Eq. (20) can be replaced with

$$p[j] = \varepsilon_j h_j + \ \sigma_j k_j \tag{22}$$

A speckle term with strength σ_j and steering vector k_j has been added in Eq. (22). In general, k_j is not parallel to h_j because the microscopic scatterers at point j that are responsible for speckle combine to scatter waves with altered phases in different directions. The degree of alteration is a property of the tissue. For some grid points in the beamforming, the altered phases at the various sensors and plane waves accidently up to a peak, like the way sidelobes form at some points when using a sparse aperture in receive beamforming. This effect creates the pattern of spots that gives speckle its name.

It is assumed that $k_j' k_j = h_j' h_j = NL$ and, for simplicity of bookkeeping, that the magnitudes of all of the elements of k_j and h_j are $\frac{1}{2}$. The length-squared of the time-sampled pressure vector is modeled as

$$\|p[j]\|^2 = \left(\varepsilon_j h_j + \ \sigma_j k_j\right)'\left(\varepsilon_j h_j + \ \sigma_j k_j\right) = \frac{NL}{4}\left(\left|\varepsilon_j\right|^2 + \left|\sigma_j\right|^2 + \frac{4}{NL} 2Re\left(\varepsilon_j^* \sigma_j h_j' k_j\right)\right) \tag{14}$$

Defining

$$s = \frac{2g'k}{\sqrt{NL}} \tag{15}$$

it can be seen that $0 \le |s|^2 \le 1$, where $|s|^2 = 0$ if $k \perp g$ and $|s|^2 = 1$ if $k \parallel g$. The coefficient $|s|^2$ plays a role similar to the relative sidelobe power in passive beamforming, except that the offending source is at the same location, $\vec{x}_j$, as the potential echogenerator of interest. In passive beamforming, a source in a different location contaminates the beamforming result with a sidelobe.

Including $\sigma_j k_j$, the pressure beamforming expression is

$$g'p = g'\left(\varepsilon_j h_j + \ \sigma_j k_j\ \right) = \frac{\sqrt{NL}}{2}\left(\varepsilon_j + \sigma_j s_j\right) \tag{16}$$

The $IQDAS$ expression becomes

$$IQDAS_j = \frac{NL}{4}\left(\varepsilon_j + \sigma_j s_j\right)\left(\varepsilon_j + \sigma_j s_j\right)^* = \frac{NL}{4}\left(\left|\varepsilon_j\right|^2 + \left|s_j\right|^2\left|\sigma_j\right|^2 + 2Re\left(\varepsilon_j^* \sigma_j s_j\right)\right) \tag{17}$$

Note that if the apodization factors w_{il} in g were all 1, then it would be the case that $g = \frac{2h_j}{\sqrt{NL}}$, so $s_j = \frac{4h_j'}{NL}$, $2Re\left(\varepsilon_j^* \sigma_j s_j\right) = \frac{4}{NL} 2Re\left(\varepsilon_j^* \sigma_j h_j' k_j\right)$, and Eq. (17) would become

$$IQDAS_j = \frac{NL}{4}\left(\left|\varepsilon_j\right|^2 + \left|s_j\right|^2\left|\sigma_j\right|^2 + \frac{4}{NL} 2Re\left(\varepsilon_j^* \sigma_j h_j' k_j\right)\right) \quad \text{(if } w_{il} \text{ are all 1)} \tag{18}$$

which is the same as Eq. (14) for $\|p[j]\|^2$ with the addition of the factor $|s_j|^2$ multiplying $|\sigma_j|^2$.

6 FUNCTIONAL BEAMFORMING

Let $\nu \geq 1$ be the Functional Beamforming (FB) exponent. The FB expression analogous to the formula in the passive beamforming case is defined by

$$b_\nu(g_j, p_j) = \left[g' C^{\frac{1}{\nu}} g\right]^\nu \tag{19}$$

Applying the spectral mapping theorem, $C^{\frac{1}{\nu}}$ is has only one nonzero eigenvalue, $\|p\|^2$, with corresponding eigenvector $\frac{p}{\|p\|}$. Eq. (11) reduces to

$$\begin{aligned} b_\nu(g_j, p_j) &= \left[g' \|p\|^{\frac{2}{\nu}} \left(\frac{p}{\|p\|}\frac{p'}{\|p\|}\right) g\right]^\nu \\ &= \|p\|^2 \left|g' \frac{p}{\|p\|}\right|^{2\nu} \\ &= \|p\|^2 \cos^{2\nu}\varphi \end{aligned} \tag{20}$$

where $\cos^2\varphi \equiv \left|g' \frac{p}{\|p\|}\right|^2$. It is not necessary to use eigenvalue decomposition software, and the processing time is exactly the same as DAS, since the computation of $\|p\|^2$ and raising the magnitude-squared of the inner product, the "sum" to the power ν are trivial.

Since $\cos^2\varphi$ for measured data p is unlikely to be 1, increasing ν decreases the BF result. The intention is that this reduces the effect of speckle and sidelobes, ideally while preserving an accurate estimate of $|\varepsilon_j|^2$.

The middle form of Eq. (17) can be written

$$b_\nu(g_j, p_j) = |g'p|^2 \left(\frac{|g'p|^2}{\|p\|^2}\right)^{\nu-1} \tag{21}$$

Using Eq. (14) and (17) in this gives

$$b_\nu = \frac{NL}{4}\left(|\varepsilon_j|^2 + |s_j|^2|\sigma_j|^2 + 2Re\left(\varepsilon_j^* \sigma_j s_j\right)\right)\left(\frac{|\varepsilon_j|^2 + |s_j|^2|\sigma_j|^2 + 2Re\left(\varepsilon_j^* \sigma_j s_j\right)}{|\varepsilon_j|^2 + |\sigma_j|^2 + \frac{4}{NL} 2Re\left(\varepsilon_j^* \sigma_j h_j' k_j\right)}\right)^{\nu-1} \tag{22}$$

To simplify this for the purpose of evaluating the effect of ν, it is convenient to ignore the cross terms, giving

$$b_\nu = \frac{NL}{4}\left(|\varepsilon_j|^2 + |s|^2|\sigma_j|^2\right)\left(\frac{|\varepsilon_j|^2 + |s|^2|\sigma_j|^2}{|\varepsilon_j|^2 + |\sigma_j|^2}\right)^{\nu-1} \tag{23}$$

At many points in an ultrasound image, there is no stricture to be visualized by $|\varepsilon_j|^2$, but the speckle $|\sigma_j|^2$ is present, creating brightness that distracts from the features to be evaluated. At such points, the second factor in Eq. (23) will be < 1, and choosing $\nu > 1$ will darken these points. However, if $|\sigma_j|^2$ is large compared with $|\varepsilon_j|^2$ and $|s|^2$ is small, then large ν could reduce b_ν below the desired value, $\frac{NL}{4}|\varepsilon_j|^2$. In practice, ν is a knob to be adjusted when viewing an ultrasound image in real time. The best choice will show the features of interest while suppressing the distractions.

To evaluate the feasibility of finding an optimum ν, Fig. 5 shows contour plots of $\frac{b_\nu}{\left(\frac{NL}{4}\right)|\varepsilon_j|^2}$ in dB as a function of ν on the horizontal axis and $10\log_{10}\left(1+\frac{|\sigma_j|^2}{|\varepsilon_j|^2}\right)$ on the vertical axis. The ideal value on the plot is 0 dB. In points where $10\log_{10}\left(\frac{b_\nu}{\left(\frac{NL}{4}\right)|\varepsilon_j|^2}\right)$ is greater that 0 dB , speckle is potentially masking $|\varepsilon_j|^2$. At points below 0 dB, overuse of ν is reducing the echogenicity shown. The optimum value of ν is seen to be quite low, about 1.05, but very effective. A somewhat higher optimum, about 1.2 – 1.5, is suggested by the real data studied in the following.

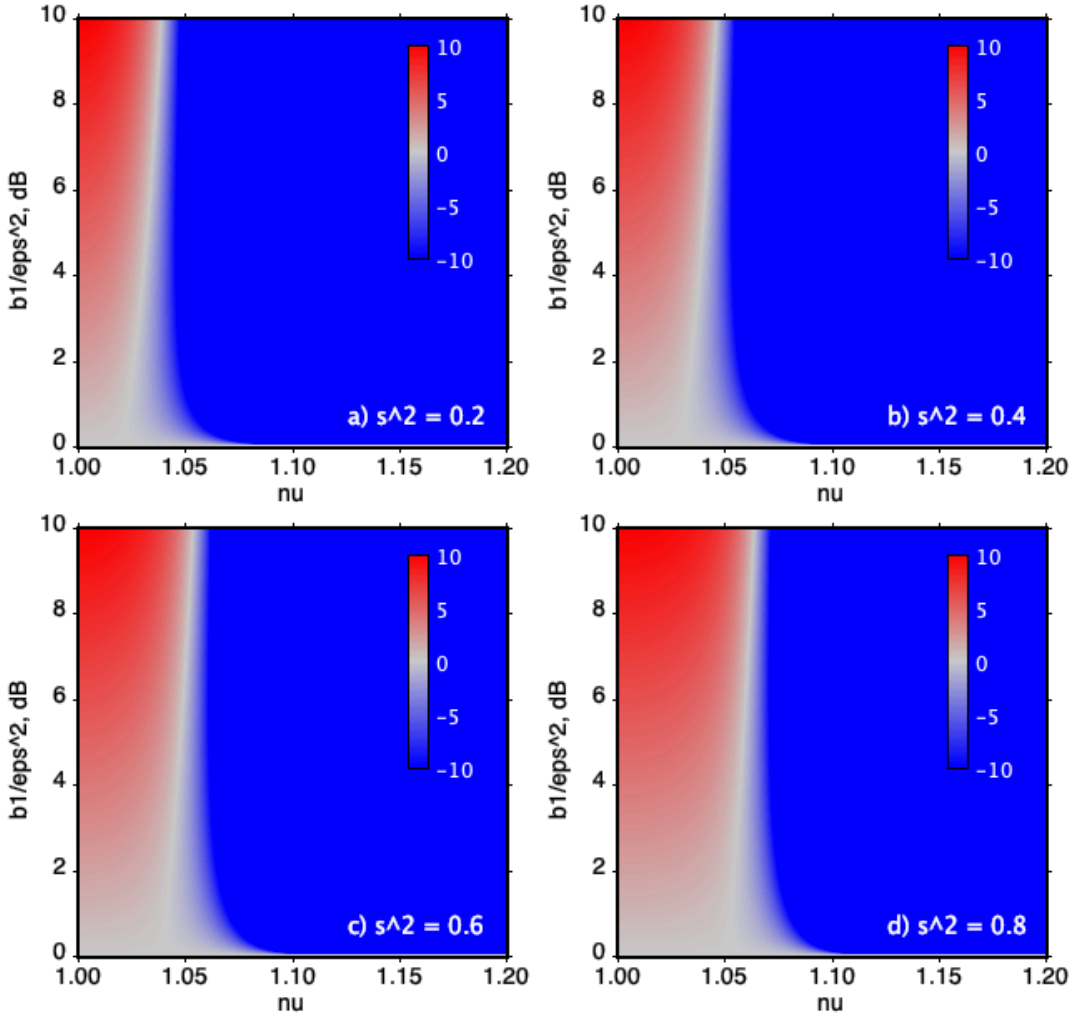

Fig. 5. Plots of the ratio of the Functional Beamfoming result in a simplified model (Eq. 9) to the correct value, in dB. Vaues above 0 dB are contaminated by speckle and values below 0 dB have been reduced too much by FB. Four values of $|s|^2$, the degree to which the speckle steering vector is parallel to the monopole steering vector, are simulated.

7 ADAPTIVE BEAMFORMING

Several workers have applied adaptive beamforming to ultrasound by averaging C over several subarrays to increase the rank of C and then inverting the different values of C for each grid point. This is a lot of computation for a method that needs to run at 100 frames per second or so. The method reduces the aperture to make sub arrays potentially reducing the resolution. The approach proposed here is to observe that the regularized version of the rank-1 matrix, $p[j]p'[j] + \lambda I$, can be inverted analytically.

First let $pp' + \lambda I = \|p\|^2 \left(\frac{p}{\|p\|}\frac{p'}{\|p\|} + \gamma I\right)$ where $\gamma = \frac{\lambda}{\|p\|^2}$. The inverse of $\left(\frac{p}{\|p\|}\frac{p'}{\|p\|} + \gamma I\right)$ is found by constructing its eigenvalue decomposition. The first eigenvector is $u_1 = \frac{p}{\|p\|}$, with eigenvalue $1 + \gamma$. The second eigenvector is formed by the Gram-Schmidt method from g, making it orthogonal to u_1:

$$u_2 = \frac{g - u_1' g u_1}{\sqrt{1 - |u_1' g|^2}} \tag{24}$$

The second eigenvalue is $u_2' \left(\frac{p}{\|p\|}\frac{p'}{\|p\|} + \gamma I\right) u_2 = \gamma$. The remaining eigenvectors, $u_3, \ldots, u_{NL}$, will not be needed explicitly. The inverse becomes

$$\left(\frac{p}{\|p\|}\frac{p'}{\|p\|} + \gamma I\right)^{-1} = \frac{1}{1+\gamma} u_1 u_1' + \frac{1}{\gamma} u_2 u_2' + \sum_{il=3}^{NL} \frac{1}{\gamma} u_{il} u_{il}' \tag{25}$$

Also needed is

$$\left(\frac{p}{\|p\|}\frac{p'}{\|p\|} + \gamma I\right)^{-2} = \frac{1}{(1+\gamma)^2} u_1 u_1' + \frac{1}{\gamma^2} u_2 u_2' + \sum_{il=3}^{NL} \frac{1}{\gamma^2} u_{il} u_{il}' \tag{26}$$

In terms of the new variables, the RAB expression is

$$b_{RAB} = \|p\|^2 \left[\frac{1}{g' \left(\frac{p}{\|p\|}\frac{p'}{\|p\|} + \gamma I\right)^{-1} g} - \gamma \frac{g' \left(\frac{p}{\|p\|}\frac{p'}{\|p\|} + \gamma I\right)^{-2} g}{\left[g' \left(\frac{p}{\|p\|}\frac{p'}{\|p\|} + \gamma I\right)^{-1} g \right]^2} \right] \tag{27}$$

Inserting Eqs. (17) & (18) into Eq. (19), terms $g' u_1 u_1' g = cos^2\varphi$ and $g' u_2 u_2' g = 1 - cos^2\varphi = sin^2\varphi$ appear. The result becomes

$$b_{RAB} = \|p\|^2 \left[\frac{1}{\frac{cos^2\varphi}{1+\gamma} + \frac{sin^2\varphi}{\gamma}} - \gamma \frac{\frac{cos^2\varphi}{(1+\gamma)^2} + \frac{sin^2\varphi}{\gamma^2}}{\left[\frac{cos^2\varphi}{1+\gamma} + \frac{sin^2\varphi}{\gamma}\right]^2} \right] \tag{28}$$

Both FB and AB take the form functions of $cos^2\varphi$ in this rank-1 version of the methods. The functions are compared in Fig. 6.

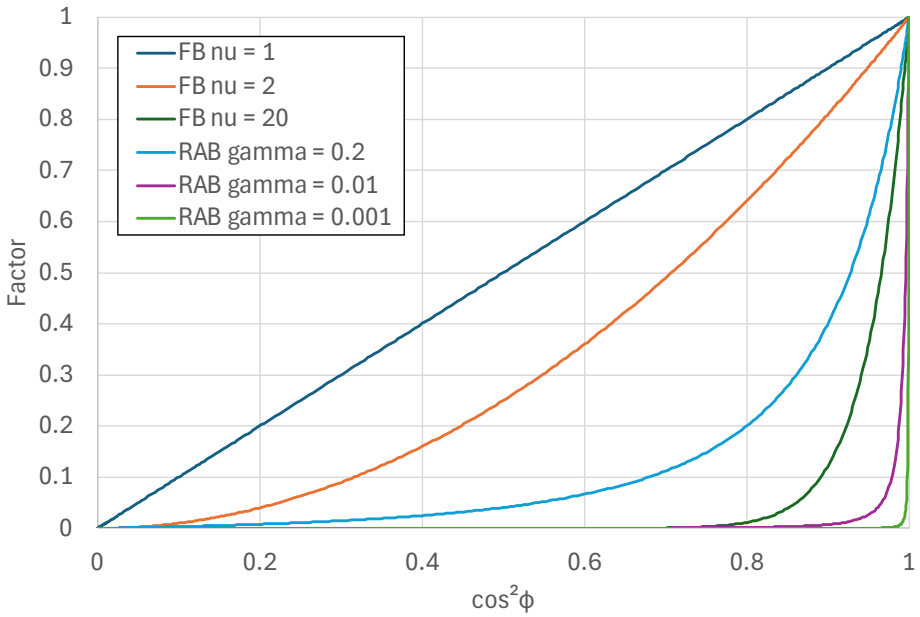

Fig. 6. Sample plots of the functions of $\cos^2\varphi$ defining FB and RAB in the rank-1 case.

8 PICMUS RESULTS

Plots from the experimental resolution phantom dataset from PICUMS are shown in Figs. 7 and 8. The B-mode images in Fig. 7 and all the 2D beamforming plots here are on a 60 dB scale. Figure 8 shows the contrast improvement and no peak loss at $\nu = 2$. This large value of ν is feasible for this data because the strong echoes from the wires in the phantom are well above the speckle. Measurement of the half-power widths of the peaks (using fits to ellipses in $x - z$) shows that the average resolution for this case is 0.44, 0.39 and 0.35 mm at $\nu = 1.0$, 1.5 and 2.0, respectively.

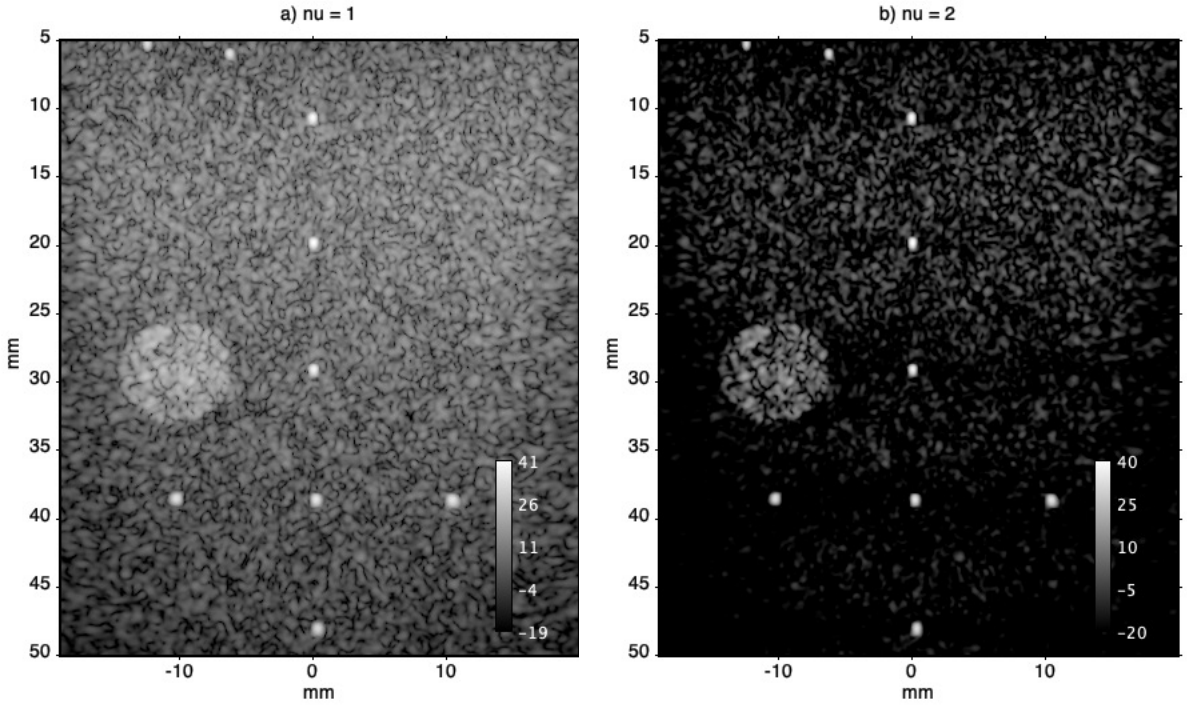

Fig. 7. DAS, a), and $\nu = 2$ FB for the experimental resolution PICMUS data.

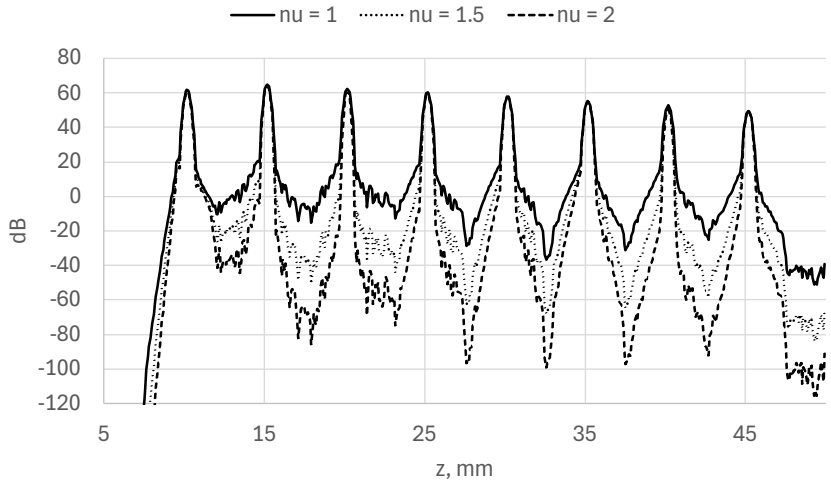

Fig. 8. Profiles of the experimental resolution PICMUS beamforming in the vertical direction.

Results for the transverse and longitudinal in-vivo PICMUS carotid artery data are shown in Figs. 9-11. The effect of ν for points along the line shown in Fig. 9a) are given in Fig. 11. The portion of the line that is most sensitive to ν is the hypoechoic lumen of the artery, This is also evident comparing the transverse plots in Fig, 10.

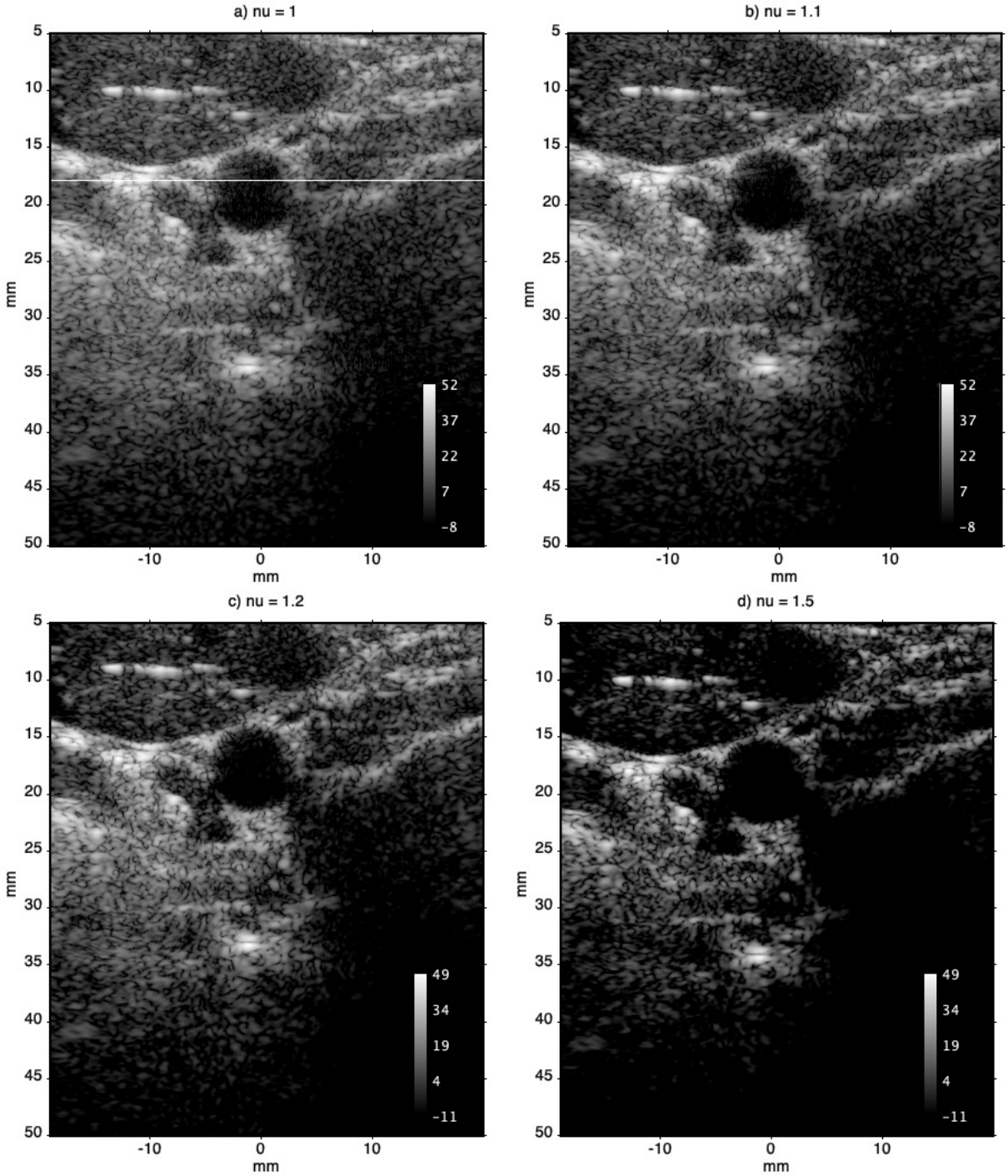

Fig. 9. DAS, a) and FB, b)-d) processing of the in-vivo PICMUS transverse carotid artery data. The horizontal line shown in a) is the cut used for the profiles in Fig. 10.

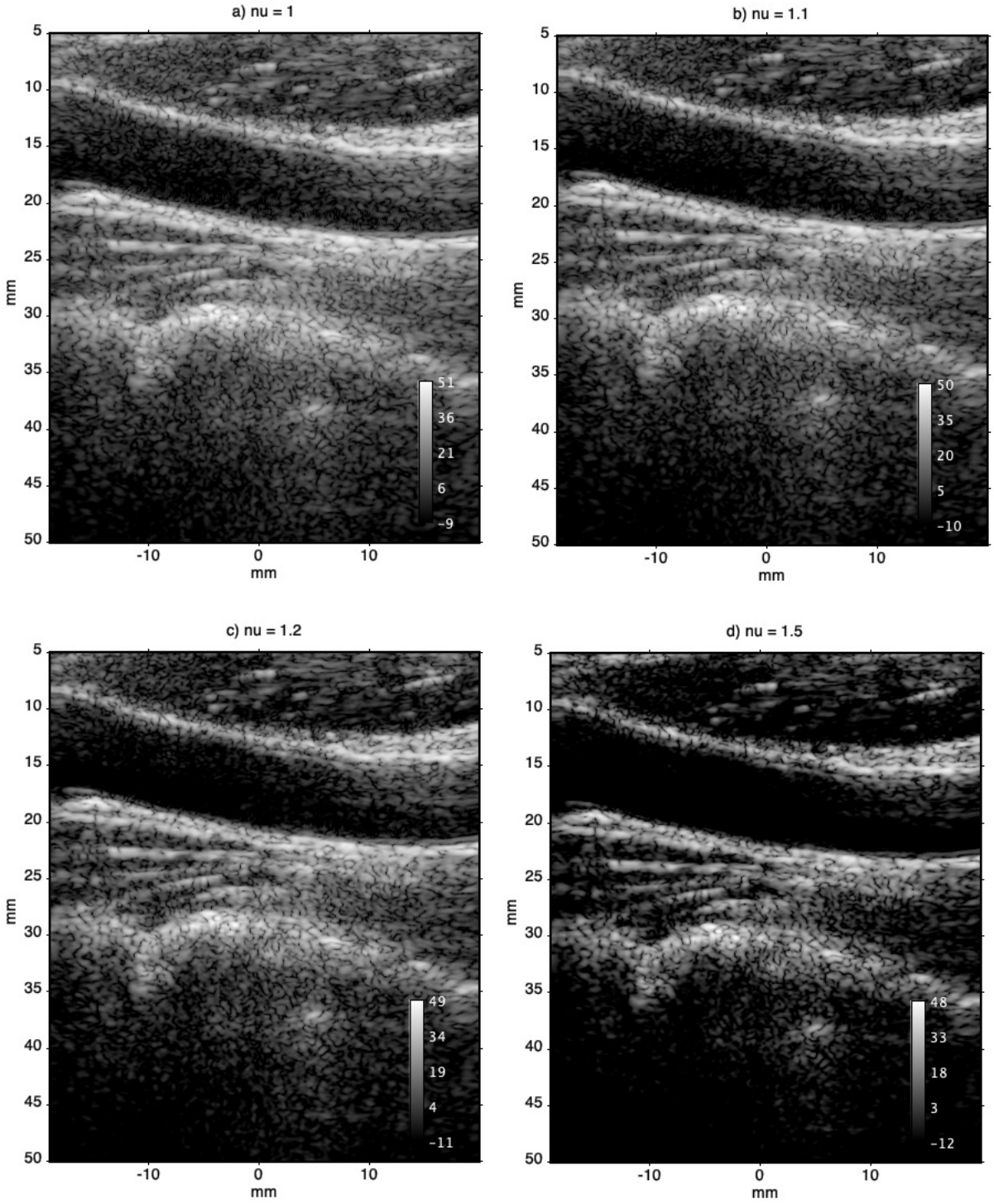

Fig.10. DAS, a) and FB, b)-d) processing of the in-vivo PICMUS longitudinal carotid artery data.

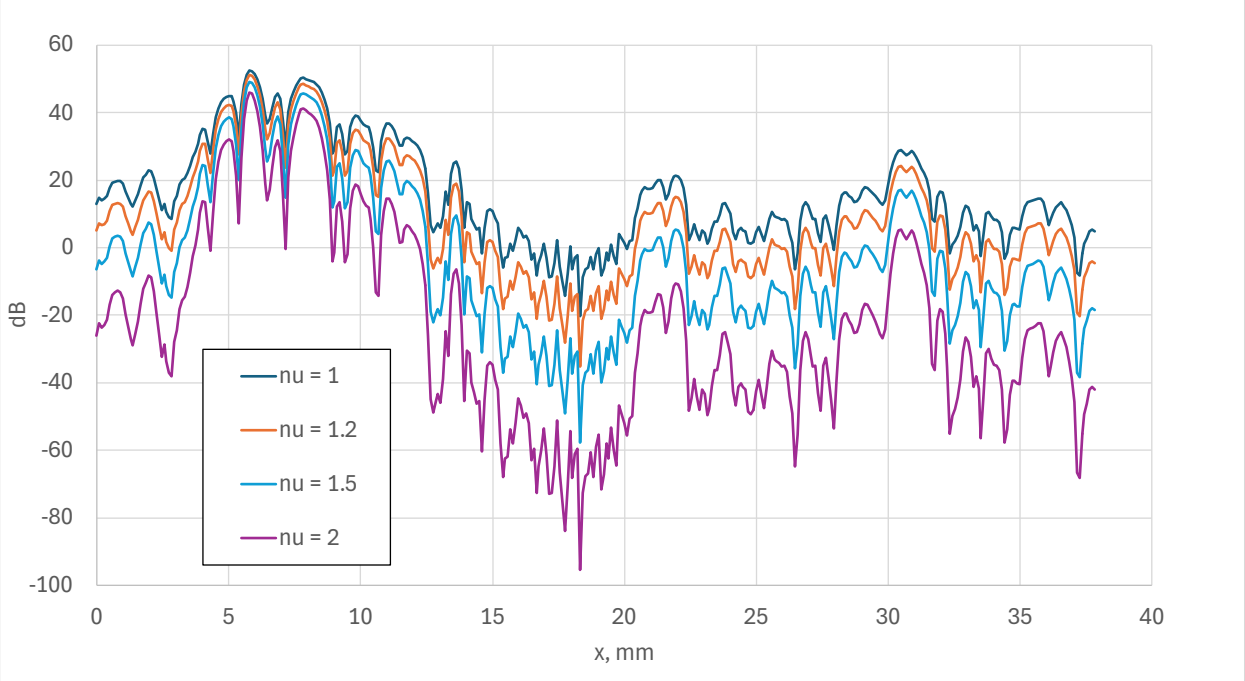

Fig. 11. Profiles of the transverse carotid artery beamforming results along the line shown in Fig. 9a). As ν increases, the results decrease monotonically at differing rates for different points along the line.

9 CONCLUSIONS

The active beamforming methods used in medical ultrasound are fundamentally different from passive beamforming. By firing a sharp pulse and selecting the data corresponding to the round-trip travel time for grid point, the array data is powerfully specialized to that grid point. Multiple plane wave excitation is used. Complex data is still used involved and advanced frequency-domain methods are available, up to a point. That point is that is only one data vector for each grid point and the CSM is therefore rank-1 unless heroic measures are taken to try to form a full rank CSM, and then it is a different CSM for each grid point! The approach used here is to work with the rank-1 CSM, which can be done very efficiently even though is depends on the grid point. Functional Beamforming was applied despite fact that the Löwner-Heinz inequality does not apply in this case, so large ν can reduce the results below the correct value. Appling the method to PICMUS sample data, effective values of ν are found in the range of 1.2-1.5, and the sample ultrasound images appear to be considerably improved. The CPU time for this method is no different from the standard method, so it will be simple and effective to put it into practice and is patent-pending. Although not explicitly tested, the method may also reduce sidelobes for sparse 2D arrays, leading to effective 3D ultrasound with a manageable channel count and computational burden. Formulas for Robust Adaptive Beamforming using the same approach are also given, although no useful results for this method have yet been obtained.

REFERENCES

[1] Montaldo G, Tanter M, Bercoff J, Benech N, Fink M. Coherent plane-wave compounding for very high frame rate ultrasonography and transient elastography.

IEEE transactions on ultrasonics, ferroelectrics, and frequency control. 2009 Apr 21;56(3):489-506.

[2] Gramann RA, Mocio JW. Aeroacoustic measurements in wind tunnels using adaptive beamforming methods. The Journal of the Acoustical Society of America. 1995 Jun 1;97(6):3694-701.

[3] Dougherty RP. Functional beamforming. In5th Berlin beamforming conference 2014 Feb 19 (pp. 19-20). GFaI, eV Berlin.

[4] Dougherty RP. Functional beamforming for aeroacoustic source distributions. In20th AIAA/CEAS aeroacoustics conference 2014 (p. 3066).

[5] Pu SL, Guo H, Xie HW, Chen C, Zhou P, Zhou GQ. Minimum variance optimizations with different covariance matrices in plane-wave ultrasound imaging. IEEE Transactions on Instrumentation and Measurement. 2024 Oct 9;73:1-3.

[6] Shen CC, Huang CL. Improvement in multi-angle plane wave image quality using minimum variance beamforming with adaptive signal coherence. Sensors. 2024 Jan 2;24(1):262.

[7] Kim, Taejin, et al. "DCL-A: An Unsupervised Ultrasound Beamforming Framework with Adaptive Deep Coherence Loss for Single Plane Wave Imaging." Diagnostics 15.24 (2025): 3193.

[8] Liebgott H, Rodriguez-Molares A, Cervenansky F, Jensen JA, Bernard O. Plane-wave imaging challenge in medical ultrasound. In2016 IEEE International ultrasonics symposium (IUS) 2016 Sep 18 (pp. 1-4). IEEE.